Letters

Enhanced Modeling of Wireless Power Transfer System With Battery Load

Xiaosheng Wang, *Student Member, IEEE*, C. Q. Jiang, *Senior Member, IEEE*, Jiayu Zhou, Liping Mo, *Member, IEEE*, and Yibo Wang

***Abstract*—This article presents an enhanced mathematical model for the wireless power transfer (WPT) system with a battery load and uncontrolled rectifier at the receiver side. The WPT system is decomposed into two subcircuits using the superposition theorem. By calculating the phase difference between the fundamental wave of the inverter output voltage and that of the rectifier input voltage, various electrical parameters including voltage, current, power, efficiency, and input impedance angle are derived. In addition, the effect of rectifier parasitic capacitance is also considered. To demonstrate its precision, the proposed model is compared with the constant-resistance and variable-resistance load models using numerical simulation software (SIMULINK) as a reliable reference. Finally, simulation and experiments are carried out to validate the theoretical analysis.**

***Index Terms*—Battery load, mathematical model, uncontrolled rectifier, wireless power transfer (WPT).**

I. Introduction

ACCURATELY modeling wireless power transfer (WPT) systems, obtaining the power characteristics, and the operational status of the system is the basis of mathematical analysis [1]. Currently, the most common approach involves directly representing the uncontrolled rectifier and battery as a parallel combination of capacitance and resistance (static load model) and utilizing fundamental harmonic analysis (FHA) [2]. To improve the accuracy of the FHA method, it is suggested that the current harmonics of the rectifier need to be considered, which will induce a phase difference between the fundamental components of the input voltage and input current of the rectifier [3], [4]. In [5], the multiple harmonics analysis (MHA) method is utilized when analyzing the variable frequency asymmetrical pulsewidth modulation, which resulted in better accuracy for judging zero-voltage switching (ZVS). However, these modeling methods are based on a static load model, where the resistance value does not change with the operating frequency and output voltage of the inverter.

The battery can be seen as a voltage source with the voltage varying with battery capacity. The WPT systems commonly use controlling the inverter's output voltage and switching frequency [2], [6]. These variations can affect the power received by the battery. Therefore, when using a resistance model to equivalent the battery load, the resistance value should vary with the operating frequency and the output voltage of the inverter. Thus, the static load model is inaccurate. The authors in [1] and [3] explained in detail the shortcomings of the static load model and presented an FHA model based on variable resistance load. The equivalent resistance was adjusted according to the voltage gain of the system and the actual output power. In addition, the phase difference between the input current and voltage of the rectifier caused by current harmonics was considered in [3]. An equivalent model consisting of a series resistance and inductance instead of the traditional constant resistance and variable resistance equivalent loads were used to achieve satisfactory precision. However, obtaining the equivalent resistance and inductance involves solving a quadratic equation. Although the authors used MATLAB's root function, solving this equation with a microcontroller would require a complex analytical solution or an additional numerical solution algorithm. Furthermore, the coefficients of this equation depend on the voltage ratio and operating frequency, necessitating the rerunning of the calculation for the equivalent resistance and inductance when the system's operating frequency or phase shift angle changes.

In addition, some researchers used the time-domain analysis method to model the WPT system [7], [8]. However, this method decomposes the system into various states and solves differential equations for each state to obtain time-domain expressions of voltage and current. The coefficients of the expressions are determined based on boundary conditions at state transition moments. Nevertheless, these results are calculated by computing the differential equation without considering the system's parasitic resistances, resulting in substantial errors when the operating

Manuscript received 27 November 2023; revised 30 December 2023 and 29 January 2024; accepted 10 February 2024. Date of publication 20 February 2024; date of current version 19 April 2024. This work was supported in part by the Science Technology and Innovation Committee of Shenzhen Municipality, China, under Grant SGDX20210823104003034, in part by the Natural Science Foundation of China (NSFC), China, under Grant 52107011, and in part by the Research Grants Council, Hong Kong SAR under ECS grant 21200622. *(Corresponding author: C. Q. Jiang.)*

Xiaosheng Wang, Jiayu Zhou, Liping Mo, and Yibo Wang are with the Department of Electrical Engineering, and the State Key Laboratory of Terahertz and Millimeter Waves, City University of Hong Kong, Hong Kong (e-mail: xiaoswang9-c@my.cityu.edu.hk; jiayzhou@cityu.edu.hk; lipingmo@cityu.edu.hk; yibo.wang@my.cityu.edu.hk).

C. Q. Jiang is with the Department of Electrical Engineering, and the State Key Laboratory of Terahertz and Millimeter Waves, City University of Hong Kong, Hong Kong, and also with the City University of Hong Kong Shenzhen Research Institute, Shenzhen 518057, China (e-mail: chjiang@cityu.edu.hk).

Color versions of one or more figures in this article are available at https://doi.org/10.1109/TPEL.2024.3367920.

Digital Object Identifier 10.1109/TPEL.2024.3367920

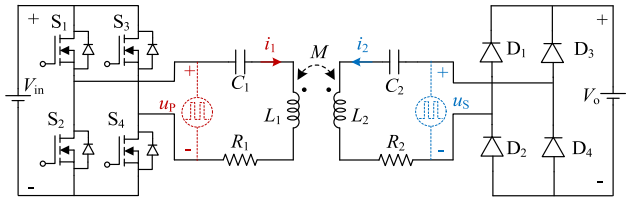

Fig. 1. Typical structure and equivalent circuit of the SS-compensated WPT system with uncontrolled rectifier and battery load (represented by a voltage source).

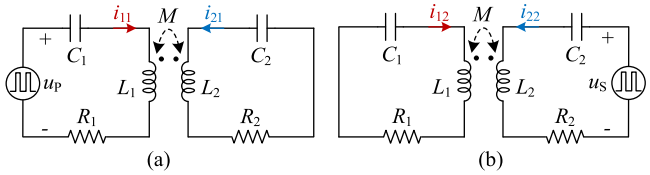

Fig. 2. Decomposition of the WPT system. (a) Subcircuit (short circuit in the receiver). (b) Subcircuit (short circuit in the transmitter).

frequency is far from the resonant frequency. Furthermore, this method requires extensive computational effort and is not a time-efficient method for obtaining frequency responses [3], [9].

This article proposes an enhanced modeling approach that offers high accuracy and does not require equation solving, making the modeling process simple and intuitive. The key innovation lies in not regarding the battery as a passive component but instead utilizing the superposition theorem to decompose the WPT systems into two subcircuits. Besides, the influence of the rectifier's parasitic capacitance is considered. By accurately determining the phase difference between the fundamental component of the inverter's output voltage and the rectifier's input voltage, various electrical parameters can be derived, including voltage, current, power, efficiency, and input impedance angle. It has potential application value in the control and optimization, parameter design for the WPT systems. Especially for some specific requirements, such as high power and misalignment tolerance, the WPT system may need to operate at zero-phase angle frequency points [10], [11].

II. Proposed Mathematical Model for Battery Loads

A. Mathematical Modeling Without Considering Parasitic Parameters

Fig. 1 presents the typical circuit of the series–series (SS) WPT systems, where u_{P} and u_{S} represent the voltages between both sides of the resonant tank. u_{S} can be regarded as a square wave with a frequency equal to switching frequency f_{s} when discontinuous conduction mode (DCM) is not considered. Input voltage and battery voltage are V_{in} and V_{o}, respectively. The coil self-inductance and resonant capacitance are L_{i} and C_{i} for the transmitter and receiver, respectively. The currents flowing through them are represented as i_1 and i_2, respectively. M represents the mutual inductance. R_1 and R_2 are the parasitic ac equivalent resistance, including the winding resistance and turn-ON resistance of the switches.

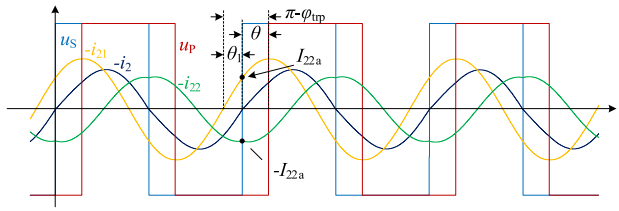

Fig. 3. Voltage and current waveform for the decomposition. ($V_{\mathrm{in}} = V_{\mathrm{out}}$, $\omega_1 = \omega_2 = 85$ kHz, $L_1 = L_2 = 107$ μH, and $\omega_{\mathrm{s}} = 95$ kHz).

Based on the superposition theorem, when the u_{P} is applied, the u_{S} should be short-circuited. Similarly, when the u_{S} is applied, the u_{P} should be short-circuited. The circuit of Fig. 1 can be decomposed into the two subcircuits shown in Fig. 2. The currents i_1 and i_2 can be represented by

$$\begin{cases} i_1 = i_{11} + i_{12} \\ i_2 = i_{21} + i_{22}. \end{cases} \tag{1}$$

Based on the KVL, the mathematic model of Fig. 2(a) can be expressed by

$$\begin{cases} \dot{U}_{\mathrm{P}} = (R_1 + jX_1)\,\dot{I}_{11} + j\omega_{\mathrm{s}} M \dot{I}_{21} \\ 0 = (R_2 + jX_2)\,\dot{I}_{21} + j\omega_{\mathrm{s}} M \dot{I}_{11}. \end{cases} \tag{2}$$

Similarly, for the subcircuit in Fig. 2(b), the equation is

$$\begin{cases} 0 = (R_1 + jX_1)\,\dot{I}_{12} + j\omega_{\mathrm{s}} M \dot{I}_{22} \\ \dot{U}_{\mathrm{S}} = (R_2 + jX_2)\,\dot{I}_{22} + j\omega_{\mathrm{s}} M \dot{I}_{12} \end{cases} \tag{3}$$

where X_1, X_2 ($X_{\mathrm{i}} = \omega_{\mathrm{s}} L_{\mathrm{i}}$-$1/\omega_{\mathrm{s}} C_{\mathrm{i}}$, $\omega_{\mathrm{s}} = 2\pi f_{\mathrm{s}}$) are the reactance of the dual side of the resonant tank. $\dot{U}_{\mathrm{P}}$ and $\dot{U}_{\mathrm{S}}$ are the phasors of the fundamental component of u_{P} and u_{S}, respectively. u_{S} can be expressed by

$$u_{\mathrm{S}}(t) = \sum_{n=1}^{N} \frac{4(V_{\mathrm{o}} + 2V_{\mathrm{d}})\sin(n\pi/2)}{n\pi} \sin(n\omega_{\mathrm{s}} t) \tag{4}$$

where V_{d} is the threshold voltage of the rectifier's diodes. According to (2) and (3), the input impedance, z_{inp} and z_{ins}, and transfer impedance z_{trp} and z_{trs} can be obtained as

$$\begin{cases} z_{\mathrm{inp}} = Z_{\mathrm{inp}} \angle \varphi_{\mathrm{inp}} = \dfrac{\dot{U}_{\mathrm{P}}}{\dot{I}_{11}} = \dfrac{M^2\omega_{\mathrm{s}}^2 + R_1 R_2 - X_1 X_2 + i(R_1 X_2 + R_2 X_1)}{R_2 + iX_2} \\ z_{\mathrm{trp}} = Z_{\mathrm{trp}} \angle \varphi_{\mathrm{trp}} = \dfrac{\dot{U}_{\mathrm{P}}}{\dot{I}_{21}} = -\dfrac{R_1 X_2 + R_2 X_1}{M\omega_{\mathrm{s}}} + \dfrac{M^2\omega_{\mathrm{s}}^2 + R_1 R_2 - X_1 X_2}{M\omega_{\mathrm{s}}}\, i \\ z_{\mathrm{ins}} = Z_{\mathrm{ins}} \angle \varphi_{\mathrm{ins}} = \dfrac{\dot{U}_{\mathrm{S}}}{\dot{I}_{22}} = \dfrac{M^2\omega_{\mathrm{s}}^2 + R_1 R_2 - X_1 X_2 + i(R_1 X_2 + R_2 X_1)}{R_1 + iX_1} \\ z_{\mathrm{trs}} = Z_{\mathrm{trs}} \angle \varphi_{\mathrm{trs}} = \dfrac{\dot{U}_{\mathrm{S}}}{\dot{I}_{12}} = -\dfrac{R_1 X_2 + R_2 X_1}{M\omega_{\mathrm{s}}} + \dfrac{M^2\omega_{\mathrm{s}}^2 + R_1 R_2 - X_1 X_2}{M\omega_{\mathrm{s}}}\, i. \end{cases} \tag{5}$$

Considering that the output power is minimal for the DCM of the uncontrolled rectifier, the mode is ignored in this article. Therefore, the u_{S} is a square wave with a 50% duty cycle. Based on the decomposition in Fig. 2, if the phase difference between the fundamental voltages of u_{P} and u_{S} can be determined, then i_1 and i_2, and many electrical parameters, including power and efficiency, can be further derived by applying the superposition theorem.

In Fig. 3, the decomposition of i_2 is presented, where ω_1 and ω_2 are the resonant frequencies of the transmitter and receiver, respectively. Since the receiver is an uncontrolled rectifier, the

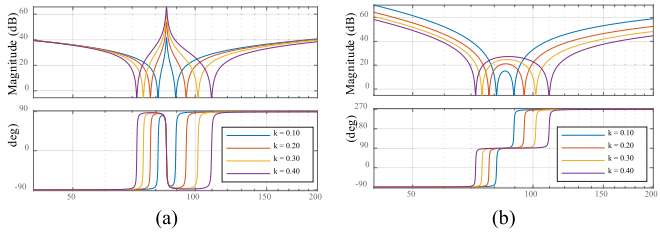

Fig. 4. Amplitude–frequency and phase–frequency characteristics of z_{inp} and z_{trp} with different k. (a) z_{inp}. (b) z_{trp}.

zero-crossing points of u_{S} and i_2 coincide when no parasitic capacitance is considered. Hence, at the zero-crossing moments of u_{S}, the instantaneous values of i_{21} and i_{22} are opposite. Due to the current harmonics, the FHA method has some errors when determining the instantaneous value ($I_{22\mathrm{a}}$) of i_{22} at the zero-crossing moments of u_{S}. Since the time domain analysis method [7], [8] can only solve differential equations without parasitic resistances R_1 and R_2 and has a significant error when the switching frequency deviates from the resonant frequency, $I_{22\mathrm{a}}$ is suggested to be directly solved by using the multiharmonic analysis [5] given by

$$I_{22a} = \sum_{n=1,3,5\ldots}^{N} \frac{4(V_{\mathrm{o}} + 2V_{\mathrm{d}})\sin(n\pi/2)\sin(-\varphi_{\mathrm{ins}}(n\omega_{\mathrm{s}}))}{n\pi Z_{\mathrm{ins}}(n\omega_{\mathrm{s}})} \tag{6}$$

where 19 for N is enough. Only odd multiple harmonics of the fundamental frequency need to be considered. Fig. 4 presents the amplitude–frequency and phase–frequency characteristics of z_{inp} and z_{trp}, where coupling coefficient k is

$$k = M/\sqrt{L_1 L_2}. \tag{7}$$

According to the amplitude–frequency characteristics shown in Fig. 4, since the coupling coefficient of the WPT systems is usually small, the S-S compensated coupler has a very strong filtering effect on the harmonics with frequency greater than $3f_{\mathrm{s}}$ (u_{S} contains harmonic components that are multiples of the fundamental frequency). i_{21} can be regarded as a sine waveform. Therefore, the phase difference θ_1 between the fundamental components of -i_{21} and u_{S} is

$$\sin\theta_1 = I_{22\mathrm{a}}/I_{21\mathrm{m}} = Z_{\mathrm{trp}} I_{22\mathrm{a}}/U_{\mathrm{Pm}} \tag{8}$$

where $I_{21\mathrm{m}}$ and U_{Pm} are the fundamental wave amplitudes of i_{21} and u_{P}, respectively. Further, the phase difference between the fundamental component of u_{P} and u_{S} can be deduced as

$$\theta = \pi - \varphi_{\mathrm{trp}} - \theta_1. \tag{9}$$

Fig. 5 shows the voltage and current phasor diagrams of the system at two switching frequencies. There is a phase difference between $\dot{U}_{\mathrm{S}}$ and $\dot{I}_2$, which shows that the traditional equivalent resistance model has some errors [3]. When I_{xx} and U_{P} are the root-mean-square values, ignoring the power transferred by the higher harmonics, the output power and input power can be

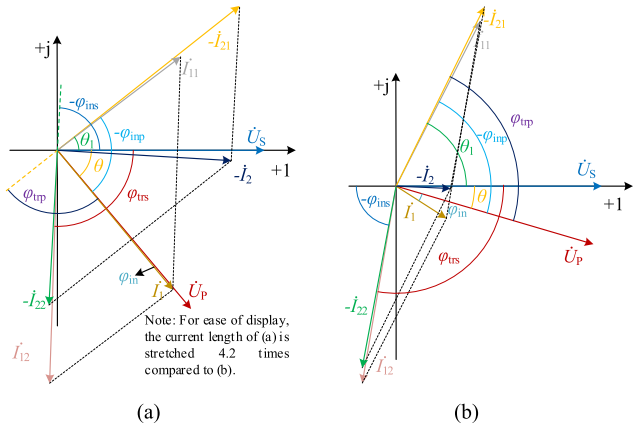

Fig. 5. Voltage and current phasor diagrams of the system. (a) $V_{\mathrm{in}} = V_{\mathrm{o}}$, $L_1 = L_2 = 107$ μH, and $f_{\mathrm{s}} = 95$ kHz. (b) $V_{\mathrm{in}} = V_{\mathrm{o}}$, $L_1 = L_2 = 107$ μH, and $f_{\mathrm{s}} = 100$ kHz.

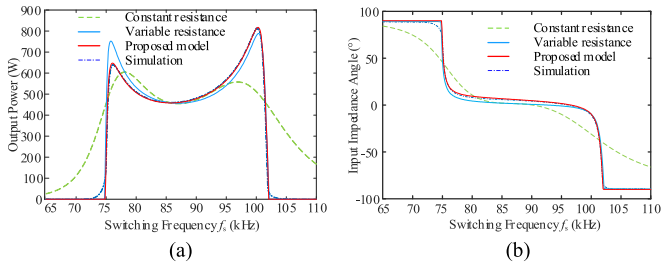

Fig. 6. Curve of output power and input impedance angle versus switching frequency. (a) Output power. (b) Input impedance angle. ($V_{\mathrm{in}} = V_{\mathrm{o}} = 100$ V, $f_1 = 85.3$ kHz, $f_2 = 84.8$ kHz, $L_1 = L_2 = 107$ μH, and $k = 0.3$).

obtained by the FHA method

$$P_{\mathrm{out}} = -\frac{8V_{\mathrm{o}}^2}{\pi^2 Z_{\mathrm{ins}}}\cos(\varphi_{ins}) - \frac{2\sqrt{2}V_{\mathrm{o}}U_{\mathrm{P}}}{\pi Z_{\mathrm{trp}}}\cos(\varphi_{\mathrm{crp}} + \theta) \tag{10}$$

$$P_{\mathrm{in}} = \frac{U_{\mathrm{P}}^2}{Z_{\mathrm{inp}}}\cos(\varphi_{\mathrm{inp}}) + \frac{2\sqrt{2}V_{\mathrm{o}}U_{\mathrm{P}}}{\pi Z_{\mathrm{trs}}}\cos(\varphi_{\mathrm{trs}} - \theta)). \tag{11}$$

Accurate calculation of input impedance angle between $\dot{U}_{\mathrm{P}}$ and $\dot{I}_1$ facilitate the analysis and implementation of ZVS. Based on the decomposition in Fig. 2, the output current $\dot{I}_1$of the inverter can be represented by

$$\dot{I}_1 = \dot{I}_{11} + \dot{I}_{12} = \frac{\dot{U}_{\mathrm{P}}}{z_{\mathrm{inp}}} + \frac{\dot{U}_{\mathrm{S}}}{z_{\mathrm{trp}}}. \tag{12}$$

Then, the input impedance angle can be calculated by

$$\varphi_{\mathrm{in}} = \arctan\left(\frac{\mathrm{Im}(\dot{I}_1 e^{j\theta})}{\mathrm{Re}(\dot{I}_1 e^{j\theta})}\right). \tag{13}$$

When the switching frequency deviates far from the resonant frequency, the DCM of the rectifier will occur, and the waveform of u_{S} will not be a square wave, affecting the calculation accuracy of θ_1 and further affecting the accuracy of the output power and input impedance angle. At this time, the power and the input impedance angle calculated by (10) and (13) will have an error, and the power may even be negative. Since the output power

of the system is very low at DCM, the adjustable switching frequency range will not deviate too much from the resonant frequency in practical applications. Therefore, when a negative output power is detected, P_{out} can be set to 0, and the φ_{in} can be directly set to -90° ($\omega_{\text{s}} > \omega_{\text{r}}$) and 90° ($\omega_{\text{s}} < \omega_{\text{r}}$). The currents i_1(t) and i_2(t) can also be derived by

$$\begin{cases} i_1 = i_{11} + i_{12} \\ = \sum_{n=1}^{N} \left(\frac{U_{\text{Pm\_n}} \sin(n\omega_{\text{s}} t + \alpha_n + n\theta - \varphi_{\text{inp}}(n\omega_{\text{s}}))}{Z_{\text{inp}}(n\omega_{\text{s}})} \right. \\ \quad \left. + \frac{U_{\text{Sm\_n}} \sin(n\omega_{\text{s}} t - \varphi_{\text{trs}}(n\omega_{\text{s}}))}{Z_{\text{trs}}(n\omega_{\text{s}})} \right) \\ i_2 = i_{21} + i_{22} \\ = \sum_{n=1}^{N} \left(\frac{U_{\text{Pm\_n}} \sin(n\omega_{\text{s}} t + \alpha_n + n\theta - \varphi_{\text{trp}}(n\omega_{\text{s}}))}{Z_{\text{trp}}(n\omega_{\text{s}})} \right. \\ \quad \left. + \frac{U_{\text{Sm\_n}} \sin(n\omega_{\text{s}} t - \varphi_{\text{ins}}(n\omega_{\text{s}}))}{Z_{\text{ins}}(n\omega_{\text{s}})} \right) \end{cases} \tag{14}$$

where $U_{\text{xm\_n}}$ is the amplitude of nth harmonic component, α_{n} is the phase angle of the nth harmonic for u_1, and α_1 is 0.

To verify the correctness of the mathematical model shown in (8)–(14), Fig. 6 shows the curves of output power and input impedance angles versus switching frequencies. Compared with the correct reference of numerical simulation, the constant resistance model has obvious errors. The variable resistance model still has some errors because of the phase difference between the fundamental component of u_{S} and i_2 caused by the harmonics. The proposed mathematical model has high accuracy and agrees well with the simulation results except when the output power is very low under DCM mode.

B. Further Corrections Considering Parasitic Parameters

Although the above proposed mathematic model is complete for the ideal WPT system, which can be seen as a simpler model based on the improvement of [3], the parasitic capacitance of diodes C_{d} as well as the total stray capacitance C_{stray} in the rectifier should be considered because the actual current value of i_2 (I_{cz}) is slightly above zero but not zero at the zero-crossing point of u_{s}. Consequently, the θ_1 and θ in (8) and (9) should be modified. When u_{s} rises from -V_{o} to 0 during Δt, where Δt is the rising time, it should be

$$0.5 I_{\text{cz}} \Delta t \approx V_{\text{o}} \left(C_{\text{d}} + C_{\text{stray}} \right). \tag{15}$$

The relationship between I_{cz} and $I_{2\text{m}}$ is approximately

$$I_{\text{cz}} \approx i'_2(t=0) \Delta t = \omega_s I_{2\text{m}} \Delta t. \tag{16}$$

I_{cz} can be approximately expressed by

$$I_{\text{cz}} \approx \omega_s I_{2\text{m}} \Delta t = \sqrt{2 V_{\text{o}} (C_{\text{d}} + C_{\text{stray}}) \omega_s I_{2\text{m}}}. \tag{17}$$

The $I_{2\text{m}}$ can be calculated by (14) using the θ_1 before modification without considering the parasitic capacitance. Therefore, the calculation of I_{cz} can be regarded as the result of an iteration with the iteration number of 1. Consequently, (8) should be modified to

$$\sin\theta_1 = \left(I_{22\text{a}} - I_{cz} \right) / I_{21\text{m}} = Z_{\text{trp}} \left(I_{22\text{a}} - I_{cz} \right) / U_{\text{Pm}}. \tag{18}$$

And then the θ will be updated based on (9). Similarly, input power, output power, and input impedance angle should also be updated when the parasitic capacitance of diodes is considered. It is worth mentioning that although the parasitic capacitance of diodes should be considered, the effect of the parasitic capacitance of the inverter's MOSFETs can be ignored. The inverter and the rectifier can be considered in a leader–follower relationship. Hence, the phase difference θ between the fundamental component of u_{P} and u_{S} has almost nothing to do with the parasitic capacitance of MOSFETs. Considering the dead time is very small, its effect on the amplitude of u_{P} can also be ignored. Besides, the line parasitic inductance and the parasitic capacitance of MOSFETs can cause high-frequency voltage spikes of u_{P} [12]. Considering the filtering characteristics of the SS coupler, the voltage spike with high frequency can hardly affect the i_1. Consequently, the effect of the parasitic capacitance of MOSFETs can be ignored.

TABLE I
SIMULATION AND EXPERIMENTAL PARAMETERS OF THE WPT SYSTEM

Parameter	Symbol	Value
Switching Frequency	f_s	65-110 kHz
Resonant Frequency of the transmitter	f_1	85.32 kHz
Resonant Frequency of the receiver	f_2	84.85 kHz
Self-inductance of the primary-side coil	L_1	107 μH
Self-inductance of the secondary-side coil	L_2	107 μH
Coupling coefficient	k	0.302, 0.491
AC resistance of the primary side	R_1	0.27 Ω
AC resistance of the secondary side	R_2	0.2 Ω
Parasitic capacitance of the reveiver	C_{d}+C_{stray}	125 pF

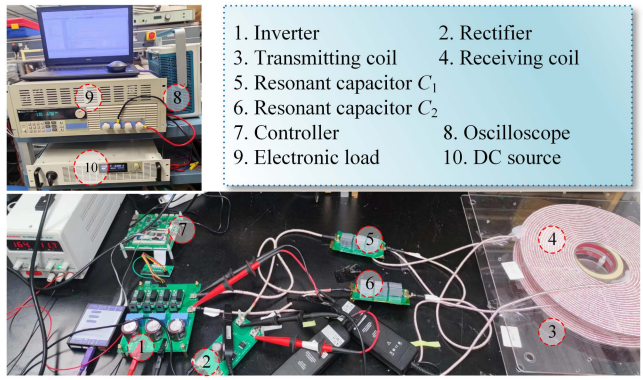

Fig. 7. Experimental prototype.

III. SIMULATION AND EXPERIMENTAL VERIFICATION

Table I presents the parameters of the simulation and experiment. The MOSFETs in the inverter are C3M0065100K, and the diodes of the rectifier are MBRB10H100. The resonant frequencies are around 85.32 and 84.85 kHz, measured by Bode 100 at the primary and secondary sides, respectively. The experimental prototype is shown in Fig. 7. To verify the accuracy of the proposed modeling method, several cases, including the static resistance load model, variable resistance load model, and the proposed model, are compared with the results of numerical simulation and experiment.

Fig. 8 presents the effect of the parasitic capacitance of diodes and MOSFETs on the output power using Simulink simulation. In

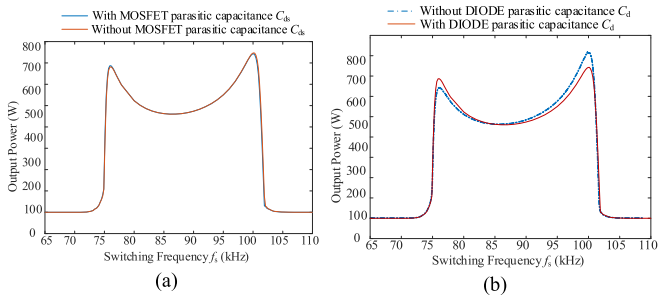

Fig. 8. Output power versus switching frequency with and without considering the parasitic capacitance of diodes and MOSFETs ($k = 0.302$). (a) Parasitic capacitance MOSFETs ($C_{ds} = 500$ pF). (b) Parasitic capacitance diodes ($C_d = 125$ pF).

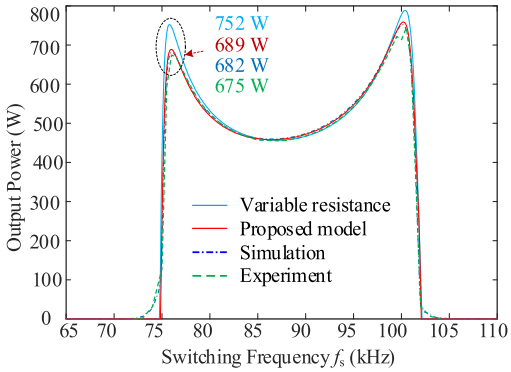

Fig. 9. Curve of output power versus switching frequency for the experiment and other models ($k = 0.302$).

TABLE II
PHASE DIFFERENCES OF u_P AND u_S FOR DIFFERENT FREQUENCIES

Phase differences	Simulation	Experiment	Variable resistance	Proposed Model
76 kHz	155.2°	156.1°	153.7°	155.9°
80 kHz	119.0°	119.1°	117.7°	120.3°
84 kHz	97.4°	97.5°	96.2°	98.4°
88 kHz	79.6°	81.9°	78.2°	80.2°
92 kHz	62.6°	62.7°	61.5°	62.6°
96 kHz	44.1°	44.4°	44.0°	44.5°

Fig. 8(a), the two plots are almost overlapping, which presents the effect of the parasitic capacitance of the MOSFETs can be ignored. However, in Fig. 8(b), there is an obvious difference between the two curves if the parasitic capacitance of diodes is compared.

Fig. 9 presents the experiment results of output power versus switching frequency. Since the parasitic capacitance of the rectifier will affect the phase difference between the u_P and u_S, the output power curve has some changes compared with Fig. 6. Compared with the variable resistance model (752 W for the left peak), the proposed model (689 W) shows better consistency with simulation (682 W) and experimental results (675 W).

Due to the current harmonics of i_1, the input impedance angle is not easily measured experimentally. Table II tabulates the

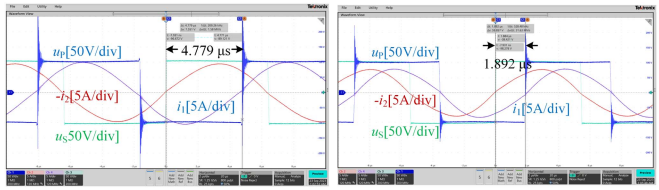

Fig. 10. Voltage and current waveform for the (a) 78 and (b) 92 kHz ($k = 0.302$).

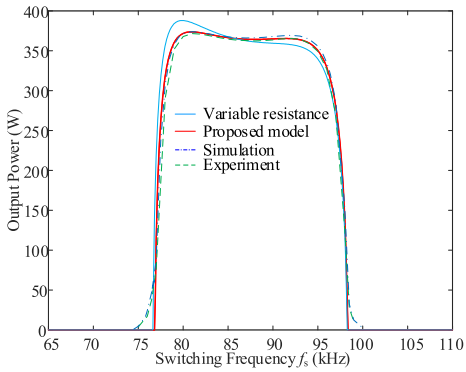

Fig. 11. Curve of output power versus switching frequency. ($V_{in} = 80$ V, $V_o = 100$ V, and $k = 0.302$).

phase differences of u_P and u_S for different frequencies. Fig. 10 presents the voltage and current waveforms at frequencies 78 and 92 kHz. The phase differences of u_P and u_S are also marked. For the 78 kHz, the phase differences are 134.1°, 134.2°, 132.2°, and 134.6° for the simulation, experiment, variable resistance model, and proposed model, respectively. For the 92 kHz, the phase differences are 62.6°, 62.7°, 61.5°, and 62.6° for the simulation, experiment, variable resistance model, and proposed model, respectively.

Fig. 11 presents the simulation and experimental results for the case when the input voltage V_{in} decreases to 80 V. The two power peaks are no longer obvious, but the power difference between the variable resistance model and the proposed model from frequency 77 to 97 kHz is significant. The proposed model can better fit the simulation and experimental results compared with the variable resistance model.

Fig. 12 presents the voltage and current waveforms with $k = 0.491$. With the increase of the coupling coefficient, there will be more current harmonics in i_2, making the phase difference between the fundamental components of u_S and i_2 larger [3], which means that the variable resistance model based on the FHA method has a larger error for the strong coupling case. Zoom in on the voltage and current waveform when the diode is turned ON. It can be observed that when the voltage crosses zero, the i_2 is slightly greater than 0, which is caused by the C_d and C_{stray}.

For the strong coupling case, the plots of the output power versus switching frequency are presented in Fig. 13. The variable resistance model has a larger error compared to the proposed model. The experimental results are in good agreement with the proposed model and simulation results.

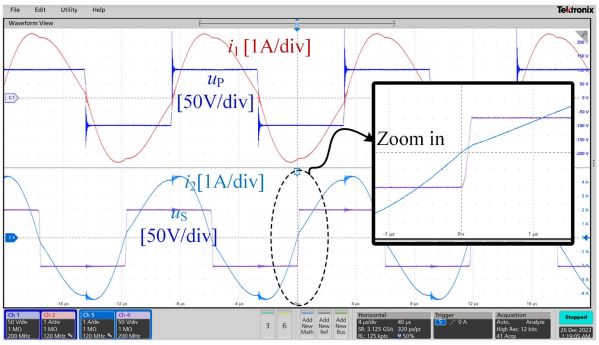

Fig. 12. Voltage and current waveform for the 85 kHz operation with $k = 0.491$.

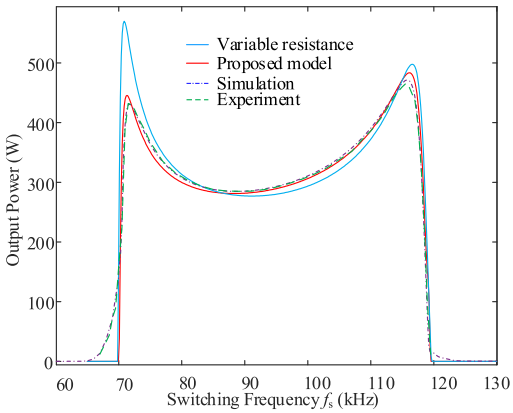

Fig. 13. Curve of output power versus switching frequency for $k = 0.491$.

TABLE III
COMPARISON WITH EXISTING METHODS

	Model	Feature	Complexity	Accuracy
[1]	Variant resistance load	Represent the receiver as varying resistance	medium	medium
[2]	Constant resistance load	Keep the load a constant resistance	low	low
[3]	Variant resistance +inductance load	Represent the receiver as varying resistance and inductance in series	high	high
[5]	MHA	Keep the load a constant resistance	medium	low
[7]	TDA	Solve differential equations	high	high
This article	Voltage source load	Solve the phase difference between u_P and u_S	medium	high

Table III compares the proposed method with the existing literature. In [2], the relationship between output power and frequency is analyzed based on the constant resistance load, resulting in much error. In [1], the variant resistance load based on the FHA method is presented, which has better accuracy than the constant resistance load. However, with the increase of the coupling coefficient, the error will increase due to the current harmonics. In [3], the receiver is represented by varying resistance and inductance in series, which has good accuracy for the battery load. However, the calculation is complex and is not direct. In [5], MHA is used to analyze a WPT system with constant resistance load, but accuracy is low for battery load. In [7], the TDA method is presented to analyze the WPT system by solving differential equations. However, the calculation process is very complicated and it is difficult to solve the WPT system when considering the ac equivalent resistance of the receiver and transmitter. For the proposed analysis method, it has good accuracy no matter weak-coupling or strong-coupling cases, and is easy to understand and calculate.

IV. CONCLUSION

This article presents an enhanced modeling method for the WPT system with an uncontrolled rectifier and battery load. The traditional constant resistance model and variable resistance model have some errors. Without a complex numerical solution of the quadratic equation, the modeling method first calculates the phase difference between u_P and u_S, and then deduces the power, input impedance angle, and current expressions. The proposed model has better coincidence with simulation and experimental results. Besides, the effect of the parasitic capacitance of the uncontrolled rectifier is discussed and considered to further regulate the model.

REFERENCES

[1] G. Guidi and J. A. Suul, "Minimizing converter requirements of inductive power transfer systems with constant voltage load and variable coupling conditions," *IEEE Trans. Ind. Electron.*, vol. 63, no. 11, pp. 6835–6844, Nov. 2016.

[2] X. Liu, X. Yuan, C. Xia, and X. Wu, "Analysis and utilization of the frequency splitting phenomenon in wireless power transfer systems," *IEEE Trans. Power Electron.*, vol. 36, no. 4, pp. 3840–3851, Apr. 2021.

[3] A. Namadmalan, J. M. Alonso, and A. Iqbal, "Accurate fundamental harmonic modeling of inductive power transfer battery chargers," *IEEE Trans. Transp. Electrific.*, vol. 8, no. 1, pp. 627–635, Mar. 2022.

[4] J. Hou, Q. Chen, X. Ren, X. Ruan, S.-C. Wong, and C. K. Tse, "Precise characteristics analysis of series/series-parallel compensated contactless resonant converter," *IEEE J. Emerg. Sel. Topics Power Electron.*, vol. 3, no. 1, pp. 101–110, Mar. 2015.

[5] Y. Fang and B. M. H. Pong, "Multiple harmonics analysis for variable frequency asymmetrical pulsewidth-modulated wireless power transfer systems," *IEEE Trans. Ind. Electron.*, vol. 66, no. 5, pp. 4023–4030, May 2019.

[6] Y. Jiang, L. Wang, Y. Wang, J. Liu, M. Wu, and G. Ning, "Analysis, design, and implementation of WPT system for EV's battery charging based on optimal operation frequency range," *IEEE Trans. Power Electron.*, vol. 34, no. 7, pp. 6890–6905, Jul. 2019.

[7] A. Safaee and K. Woronowicz, "Time-domain analysis of voltage-driven series–series compensated inductive power transfer topology," *IEEE Trans. Power Electron.*, vol. 32, no. 7, pp. 4981–5003, Jul. 2017.

[8] Y. Zhang, X. Li, S. Chen, and Y. Tang, "Soft switching for strongly coupled wireless power transfer system with 90° dual-side phase shift," *IEEE Trans. Ind. Electron.*, vol. 69, no. 1, pp. 282–292, Jan. 2022.

[9] A. K. Rathore and V. R. Vakacharla, "A simple technique for fundamental harmonic approximation analysis in parallel and series–parallel resonant converters," *IEEE Trans. Ind. Electron.*, vol. 67, no. 11, pp. 9963–9968, Nov. 2020.

[10] J. Zhou, B. Zhang, W. Xiao, D. Qiu, and Y. Chen, "Nonlinear parity-time-symmetric model for constant efficiency wireless power transfer: Application to a drone-in-flight wireless charging platform," *IEEE Trans. Ind. Electron.*, vol. 66, no. 5, pp. 4097–4107, May 2019.

[11] S. Assawaworrarit, X. Yu, and S. Fan, "Robust wireless power transfer using a nonlinear parity–time-symmetric circuit," *Nature*, vol. 546, pp. 387–390, Jun. 2017.

[12] X. Yang, M. Xu, Q. Li, Z. Wang, and M. He, "Analytical method for RC snubber optimization design to eliminate switching oscillations of SiC MOSFET," *IEEE Trans. Power Electron.*, vol. 37, no. 4, pp. 4672–4684, Apr. 2022.